Turbulence suppression by cardiac-cycle-inspired driving of pipe flow

D. Scarselli[1], J. M. Lopez[1,2], A. Varshney[1,3] & B. Hof[1]

[1]*Institute of Science and Technology Austria, 3400 Klosterneuburg, Austria*

[2]*Universidad de Málaga, Campus de Teatinos, s/n, 29071, Málaga, Spain*

[3]*School of Physical Sciences, National Institute of Science Education and Research, HBNI, Jatni-752050, Odisha, India*

Flows through pipes and channels are in practice almost always turbulent, and the multiscale eddying motion is responsible for the major part of the encountered friction losses and pumping costs[1]. Conversely, for pulsatile flows, in particular for aortic blood flow, turbulence levels remain surprisingly low despite relatively large peak velocities. Indeed, in this latter case, high turbulence levels are intolerable as they would damage the shear sensitive endothelial cell layer[2–5]. We here show that turbulence in ordinary pipe flow is diminished if the flow is driven in a pulsatile mode that incorporates all the key features of the cardiac waveform. At Reynolds numbers comparable to aortic blood flow, turbulence is largely inhibited, whereas, at much higher speeds, the turbulent drag is reduced by more than 25%. This specific operation mode is more efficient when compared to steady driving, which is the status quo for virtually all fluid transport processes ranging from heating circuits to water, gas and oil pipelines.

Turbulent flows are ubiquitous in nature and applications and are associated with large fric-

tion levels and high pumping costs when compared to laminar conditions. Available estimates show that around 10% of global electric power is consumed for pumping fluids [6]. In this context, turbulence is not only encountered at large scales, such as in oil or gas pipelines, but equally dominates flows in domestic settings (e.g. in heating pipes or the flow from a faucet). Even aortic blood flow in humans and large mammals periodically exceeds transition thresholds. Compared to a transition Reynolds number of $Re_c \approx 2\,040$ [7], aortic peak Reynolds numbers in humans reach more than twice[8,9] this value, while in equine aortas peak values of $10\,000$ are common[10]. In the cardiovascular context, high turbulence levels constitute a severe health hazard, as intense fluctuations and varying shear stresses are attributed to endothelial cell dysfunction and arteriosclerosis[2–5].

In engineering applications, in addition to the excessive drag levels, fluctuations and alternating shear stresses can equally have adverse effects, and much effort has been dedicated to developing means to control turbulence. However, despite many novel and innovative approaches[11], so far, a broadly applicable method remains elusive. Active control techniques[12–14] require complex actuation devices[15,16], and in experimental realisations, the costs often far exceed the gains. Passive approaches equally suffer from high implementation costs and typically have a limited operation range[1,17]. Additives, such as long chain polymers, degrade over time[18,19] and contaminate liquids. Available control techniques are hence problem specific and intrusive, requiring either manipulation of fluid properties or costly and often impractical implementations. Conversely, aortic flow provides an example where a specific propulsion scheme, consisting of impulsive bursts separated by quiescent intervals, appears to hold turbulence at bay despite relatively large peak velocities.

The effect of unsteady, pulsatile driving on turbulence has been extensively investigated in experiments and numerical simulations[20–26]. In these studies, an initially steady turbulent flow undergoes a periodic change in fluid speed, and the statistical properties of the evolving flow are investigated. Flow acceleration typically delays turbulent kinetic energy production and decreases the wall shear stress with respect to the quasi-steady value. Deceleration, on the other hand, enhances friction, although at higher deceleration rates, there is evidence of friction reduction[27]. Recent numerical studies[28,29] identified unsteady driving conditions that can result in considerable drag reduction, although the proposed numerical strategies are not necessarily straightforward to implement in experiments in practice.

In this present study, we present an alternative approach to turbulence control, where drag reduction is achieved by means of unsteady, pulsatile driving, specifically mimicking the cardiac cycle and extending this method to large Reynolds numbers.

Experiments are carried out in a $1.2\,\text{m}$ long pipe (inner diameter $D = 10$ mm), and water is driven through the setup by a piston. The piston speed is accurately controlled by a servo motor and allows us to alter the flow rate in time, and in particular, to realise a pulsatile flow of the desired waveform. For further details of the experimental setup, we refer the reader to the methods section . Initial experiments were carried out at moderate Reynolds numbers, values which are comparable to those in aortic blood flow. We compare three flows in the same pipe set up at identical instantaneous Reynolds number ($Re = U_{\text{m}}D/\nu$, where U_{m} is the instantaneous bulk speed in the pipe). In the first case, the flow is driven steadily at $Re = 2\,800$ and as shown in Fig. 1a

the fluid motion is turbulent throughout. In the second experiment, the flow is driven periodically using the waveform (see Fig. 1d) reported for cardiovascular flow in the descending part of a human aorta [30], choosing a peak value close to the maximum values reported in literature[31]. Even though the pipe set up is unchanged (including the inlet condition) the flow is fully laminar despite instantaneous Reynolds numbers larger than 5000 (Fig. 1**b**) . We next tested a cycle in which the diastolic rest phase was removed, as shown in Fig. 1 **e**. Compared to the cardiovascular case **d**, we down-scaled the peak velocity by a factor of 1.5 so that the average Reynolds numbers of the two cycles remain comparable. In this case, the flow indeed remains by and large turbulent, which hints at the relevance of the diastolic rest phase for turbulence suppression.

From the above experiments, it is apparent that unlike for steady driving, the state of the flow, i.e. laminar or turbulent, is not solely determined by the instantaneous Reynolds number and that the waveform plays a decisive role. If turbulence develops during a cycle also depends on the initial fluctuation level at the beginning of the cycle, and hence on the flow's history. In this respect, the diastole plays a central role, as it effectively decouples the acceleration from the prior deceleration, allowing turbulence and fluctuations to decay before Re increases again. In the following, we investigate the effect of the pulsatile operation mode on a fully turbulent flow at significantly larger time averaged Reynolds numbers $\overline{Re} = \overline{U}D/\nu$ (where $\overline{U}$ is the bulk speed averaged over one pulsation period, D the pipe diameter and ν the fluids kinematic viscosity) in order to investigate the impact of pulsation on drag. To this end, we pump water through a 7 m long pipe (inner diameter $D = 30$ mm) by means of the same syringe setup described above. The pressure drop Δp is measured across a length $L = 120\,D$ after a development length of $60\,D$ from

the pipe inlet. Subsequently, the wall shear stress τ_w is reconstructed by using the force balance in the streamwise direction

$$\rho \frac{dU_m}{dt} = -\frac{\Delta p}{L} - \frac{4\tau_w}{D}, \tag{1}$$

where ρ is the water density and U_m is the instantaneous bulk flow velocity. Experiments are accompanied by direct numerical simulations (DNS) of the Navier–Stokes equations where the identical time variation of the Reynolds number is imposed. The DNS are performed for a 5D long pipe with periodic boundary conditions using a parallel solver[32] (*NSPipeFlow*, see methods for further details).

In initial experiments and simulations, we tested a cycle consisting of a series of linear flow rate ramps smoothly joined together, corresponding to Re oscillating between $Re_{\mathrm{min}} = 3\,200$ and $Re_{\mathrm{max}} = 18\,800$ with a period $T = 4.5$ s, see Fig. 2 **a**. Note that, even for the minimum Re value, steady flows are fully turbulent in our pipe set-up.

From measurements of the pressure drop $\Delta p(t)$ and the imposed bulk velocity $U_{\mathrm{m}}(t)$ we can determine the wall shear stress using equation (1). To ease comparison between different cycles, τ_w is nondimensionalized by the dynamic pressure at the cycles' minima, corresponding to $(0.5\rho U_{\mathrm{min}}^2)$, where U_{min} is the bulk velocity at $Re = 3\,200$. We hence define $\tau^* = 2\tau_w/(\rho U_{\mathrm{min}}^2)$ and in Fig. 2 **d** the instantaneous experimental values (blue circles) are compared to the quasi–steady reference case, τ_{qs}^* (black dotted line), i.e. the wall shear stress expected if turbulence would instantaneously adjust to changes in Re. At the beginning of each cycle τ^*, although low, is considerably larger than τ_{qs}^*. Only as the flow acceleration proceeds measured values eventually fall below τ_{qs}^*, in line

5

with previous observations of drag reduction during flow acceleration.

While the instantaneous wall shear stress values indicate an overall drag reduction compared to the quasi–steady case, this does not necessarily imply drag reduction compared to a steadily driven flow of identical average Reynolds number. The drag change with respect to the steadily driven flow is

$$R = \frac{\tau_{\text{steady}}^* - \overline{\tau^*}}{\tau_{\text{steady}}^*},$$ (2)

where the overline denotes an average over several cycles, and the steady flow wall shear stress τ_{steady}^* is obtained from the Blasius[33] friction factor relation and normalised in the same manner as the cyclic flow. For the cycle of Fig. 2 **a**, the drag in experiments turns out to be 4.4% larger ($R = -0.044$) than the steady flow. It is noteworthy that the quasi–steady case $\overline{\tau_{\text{qs}}^*}$ generally has a drag considerably larger than the actual steady flow. In the present case it results in a 14% drag increase compared to τ_{steady}^*. Pulsation hence does not necessarily lead to drag reduction let alone energy saving. Inspired by the diastolic phase found in the aortic flow and the transition delay obtained for the cardiac waveform, we designed a new cycle where a region of constant Re (rest phase) is inserted that effectively decouples the deceleration from the consecutive acceleration phase (Fig. 2 **b**). Remarkably, the flow now responds with considerably lower values of τ^* during acceleration, as well as during part of the deceleration phase (Fig. 2 **e**). The peak value of τ^* is reduced by a factor of two, and in this case, we obtain a net drag reduction of 23% ($R = 0.23$). The central role of the rest phase can be understood as follows. During acceleration, turbulence remains initially frozen, i.e. variations in the mean velocity have a minimal impact on the turbulent stresses, leading to significant drag reduction. The amount of drag reduction achievable sensitively depends on the

6

turbulence level at the beginning of this acceleration phase. Conversely, during deceleration, an inflection point emerges in the velocity profile, causing turbulence levels that typically exceed those expected for the instantaneous Re value, especially by the end of this phase. The subsequent rest phase crucially allows turbulence levels to die down and hence sets a favourable initial condition for the next acceleration phase.

From an energetic point of view, in unsteady flows a reduction of the mean friction τ^* is not sufficient to ensure that the power dissipation per unit length ($P = Q\Delta p/L$, where Q is the volume flow rate) is lower with respect to steady conditions. To quantify this aspect, we introduce the power saving

$$S = \frac{P_{\text{steady}} - \overline{P}}{P_{\text{steady}}},$$ (3)

where P_{steady} is the power dissipated by the steadily driven, i.e. constant Re reference flow and $\overline{P}$ is the time averaged power dissipation of the pulsatile flow. The instantaneous values of the power dissipation are given by $P(t) = \Delta p(t)Q(t)$, where $Q(t)$ is the volume flow rate, determined from the measured instantaneous piston speed. Computing the power savings for the cycle of Fig. 2 b yields a loss ($S = -0.03$), notwithstanding the large drag reduction. The power loss is caused by the additional energy input required to accelerate the flow, since an increase of flow rate requires the pressure gradient and hence the power to grow (cf. Eq. (1)). The waveform of Fig. 2b is hence advantageous (compared to steady driving) in situations where high shear stresses are detrimental, as is the case for the endothelium, but counterproductive if energy efficiency is the main incentive. While so far we have considered waveforms with lower acceleration and higher deceleration rates (Figs. 2 **a** and **b**), the opposite holds for velocity waveforms in the aorta [30]. Correcting for this,

we chose the waveform displayed in Fig. 2 **c**, with a higher acceleration rate, while the rest phase is left unchanged. During the more rapid Re increase, friction initially increases somewhat faster than for waveform b, subsequently however, the friction drops at the beginning of the deceleration phase (Fig. 2 **f**). Here, friction reaches levels comparable to the ones assumed during the rest phase, albeit at very high Re. This effect further improves drag reduction, which now reaches 27% ($R = 0.27$). Computing the power balance, we in this case obtain a net saving of 9% ($S = 0.09$) compared to steadily driven pipe flow. Equally for the DNS, cycle Fig. 2 **c** is the only one that results in drag reduction as well as energy saving. While the amount of drag reduction in the DNS ($R = 0.28$) almost precisely matches experiments, the energy saving ($S = 0.07$) is slightly smaller. Taking into account that due to computational cost, the DNS results were averaged over a much smaller number of cycles, the agreement is nevertheless very good (see table Extended Data 2 and Fig. Extended Data 3 for a comparison of experiments and DNS).

Finally, we investigate how changing the acceleration and rest phase affects drag reduction and power savings. To this end, we carried out a total of 225 experiments spanning different rest phase and acceleration durations (denoted respectively by T_r and T_a), while keeping minimum and maximum Re and the combined duration of the acceleration and deceleration phases ($T = 0.02 \cdot 4\nu/D^2$) constant (cf. Fig. Extended Data 4). The resulting map of power saving S is shown in Fig. 3 **a**.

The white, dashed line separates the regions of positive and negative S and the cycles of Fig. 2 **a**, **b** and **c** are denoted respectively by a circle, star and square. Interestingly, shorter acceleration

times consistently lead to higher power savings, hence suggesting the importance of a brief, intense acceleration followed up by a longer, more gentle deceleration. Specifically for power saving we find that the acceleration phase has to be much shorter ($\lesssim 1\%$) than the viscous time scales of the flow. This abrupt change prohibits the flow profile's adjustment to its (high drag) quasi steady shape. Strictly, for the parameter regime investigated, a non zero rest phase is required to save power. However, there is an optimal rest phase and longer rest phases are counterproductive. The optimal value of T_r depends weakly on T_a and it is approximately equal to half the duration of the unsteady part of the cycle ($t \cdot 4\nu/D^2 \approx 0.01$). Remarkably, with $T_r^{\text{heart}} \cdot 4\nu/D^2 \approx 0.012$, the rest phase observed for the aortic cycle in humans is close to this value.

The same parameter space can be mapped to the usual f–$\overline{Re}$ plane, where $f = 2D\Delta p/\left(\rho \bar{U}^2 L\right)$ is the Darcy friction factor (Fig. 3 **b**), to highlight the effect of the cycles on the drag reduction R and the dependence on $\overline{Re}$. For comparison, we plot the Blasius relation for turbulent friction. The largest reduction in f (27% drag reduction) is found for $\overline{Re} \approx 8\,600$ and it is close to the region of maximum S.

The circulatory system manages to combine flow speeds, significantly exceeding onset values of turbulence, with low shear stress levels. Sufficient flow rates are crucial for a functioning organism, while at the same time, the stress levels have to remain tolerable for the blood vessels' endothelial cell layer. As we have shown, the waveform of the cardiac cycle is close to optimal to achieve both of these objectives. A rest phase during the cycle is crucial to diminish wall shear stress and, at the same time, this rest phase has to be optimally timed and combined with a sub-

sequent rapid flow acceleration to not only reduce the flow drag but to also optimize its efficiency and minimize power consumption.

Fluid transport is one of the largest sources of energy consumption in present day societies and a major part of pumping costs can be attributed to turbulence. While pipeline flows are commonly run at a steady flow rate, our study demonstrates that, from an energetic point of view, this is not necessarily the optimal operation mode.

Acknowledgments

Author Contributions

B.H. supervised the project. D.S. and A.V. designed and performed the experiment. D.S. analyzed the experimental data. J.M.L. designed and performed the computer simulations of the Navier–Stokes equations and analysed the numerical results. D.S., J.M.L., A.V. and B.H. wrote the paper.

Author Information

References

1. Kühnen, J. *et al.* Destabilizing turbulence in pipe flow. *Nat. Phys.* **14**, 386–390 (2018).

2. Davies, P. F., Remuzzi, A., Gordon, E. J., Dewey, C. F. & Gimbrone, M. A. Turbulent fluid shear stress induces vascular endothelial cell turnover in vitro. *Proc. Natl Acad. Sci. USA* **83**, 2114–2117 (1986).

3. DePaola, N., Gimbrone, M. A., Davies, P. F. & Dewey, C. F. Vascular endothelium responds to fluid shear stress gradients. *Arterioscler. Thromb. J. Vasc. Biol.* **12**, 1254–1257 (1992).

4. Davies, P. F. Hemodynamic shear stress and the endothelium in cardiovascular pathophysiology. *Nat. Clin. Pract. Cardiovasc. Med.* **6**, 16–26 (2009).

5. Gimbrone, M. A. & García–Cardeña, G. Endothelial Cell Dysfunction and the Pathobiology of Atherosclerosis. *Circ. Res.* **118**, 620–636 (2016).

6. Frenning, L. *Pump Life Cycle Costs: A Guide to LCC Analysis for Pumping Systems* (Hydraulic Institute, 2001).

7. Avila, K. *et al.* The Onset of Turbulence in Pipe Flow. *Science* **333**, 192–196 (2011).

8. Ku, D. N. *et al.* Blood flow in arteries. *Annual review of fluid mechanics* **29**, 399–434 (1997).

9. Stalder, A. F. *et al.* Assessment of flow instabilities in the healthy aorta using flow-sensitive mri. *Journal of magnetic resonance imaging* **33**, 839–846 (2011).

10. Nerem, R. M., Rumberger Jr, J. A., Gross, D. R., Hamlin, R. L. & Geiger, G. L. Hot-film anemometer velocity measurements of arterial blood flow in horses. *Circulation research* **34**, 193–203 (1974).

11. Brunton, S. L. & Noack, B. R. Closed-loop turbulence control: Progress and challenges. *Applied Mechanics Reviews* **67** (2015).

12. Karniadakis, G. & Choi, K.-S. Mechanisms on Transverse Motions in Turbulent Wall Flows. *Annu. Rev. Fluid Mech.* **35**, 45–62 (2003).

13. Min, T., Kang, S. M., Speyer, J. L. & Kim, J. Sustained sub–laminar drag in a fully developed channel flow. *J. Fluid Mech.* **558**, 309–318 (2006).

14. Nakanishi, R., Mamori, H. & Fukagata, K. Relaminarization of turbulent channel flow using traveling wave–like wall deformation. *Int. J. Heat Fluid Flow* **35**, 152–159 (2012).

15. Auteri, F., Baron, A., Belan, M., Campanardi, G. & Quadrio, M. Experimental assessment of drag reduction by traveling waves in a turbulent pipe flow. *Phys. Fluids* **22**, 115103 (2010).

16. Kasagi, N., Suzuki, Y. & Fukagata, K. Microelectromechanical Systems–Based Feedback Control of Turbulence for Skin Friction Reduction. *Annu. Rev. Fluid Mech.* **41**, 231–251 (2009).

17. Garcia-Mayoral, R. & Jiménez, J. Drag reduction by riblets. *Philos. Trans. R. Soc. Math. Phys. Eng. Sci.* **369**, 1412–1427 (2011).

18. Virk, P. S., Mickley, H. S. & Smith, K. A. The Ultimate Asymptote and Mean Flow Structure in Toms' Phenomenon. *J. Appl. Mech.* **37**, 488–493 (1970).

19. Choueiri, G. H., Lopez, J. M. & Hof, B. Exceeding the Asymptotic Limit of Polymer Drag Reduction. *Phys. Rev. Lett.* **120**, 124501 (2018).

20. He, S. & Jackson, J. D. A study of turbulence under conditions of transient flow in a pipe. *J. Fluid Mech.* **408**, 1–38 (2000).

21. Greenblatt, D. & Moss, E. A. Rapid temporal acceleration of a turbulent pipe flow. *J. Fluid Mech.* **514**, 65–75 (2004).

22. He, S., Ariyaratne, C. & Vardy, A. E. Wall shear stress in accelerating turbulent pipe flow. *J. Fluid Mech.* **685**, 440–460 (2011).

23. He, S. & Seddighi, M. Turbulence in transient channel flow. *J. Fluid Mech.* **715**, 60–102 (2013).

24. He, K., Seddighi, M. & He, S. DNS study of a pipe flow following a step increase in flow rate. *Int. J. Heat Fluid Flow* **57**, 130–141 (2016).

25. Mathur, A. *et al.* Temporal acceleration of a turbulent channel flow. *J. Fluid Mech.* **835**, 471–490 (2018).

26. Cheng, Z., Jelly, T., Illingworth, S., Marusic, I. & Ooi, A. Forcing frequency effects on turbulence dynamics in pulsatile pipe flow. *International Journal of Heat and Fluid Flow* **82**, 108538 (2020).

27. Ariyaratne, C., He, S. & Vardy, A. E. Wall friction and turbulence dynamics in decelerating pipe flows. *J. Hydraul. Res.* **48**, 810–821 (2010).

28. Kobayashi, W., Shimura, T., Mitsuishi, A., Iwamoto, K. & Murata, A. Prediction of the drag reduction effect of pulsating pipe flow based on machine learning. *International Journal of Heat and Fluid Flow* **88**, 108783 (2021). URL https://www.sciencedirect.com/science/article/pii/S0142727X21000138.

29. Foggi Rota, G., Monti, A., Rosti, M. E. & Quadrio, M. Saving energy in turbulent flows with unsteady pumping. *Scientific Reports* **13**, 1299 (2023).

30. Bürk, J. *et al.* Evaluation of 3D blood flow patterns and wall shear stress in the normal and dilated thoracic aorta using flow–sensitive 4D CMR. *J Cardiovasc Magn Reson* **14**, 84 (2012).

31. Stein, P. D. & Sabbah, H. N. Turbulent blood flow in the ascending aorta of humans with normal and diseased aortic valves. *Circulation research* **39**, 58–65 (1976).

32. López, J. M. *et al.* nscouette – a high-performance code for direct numerical simulations of turbulent taylor–couette flow. *SoftwareX* **11**, 100395 (2020). URL https://www.sciencedirect.com/science/article/pii/S2352711019302298.

33. Blasius, H. Das Ähnlichkeitsgesetz bei Reibungsvorgängen in Flüssigkeiten. *Mitteilungen Über Forschungsarbeiten Auf Dem Geb. Ingenieurwesens* **131** (1913).
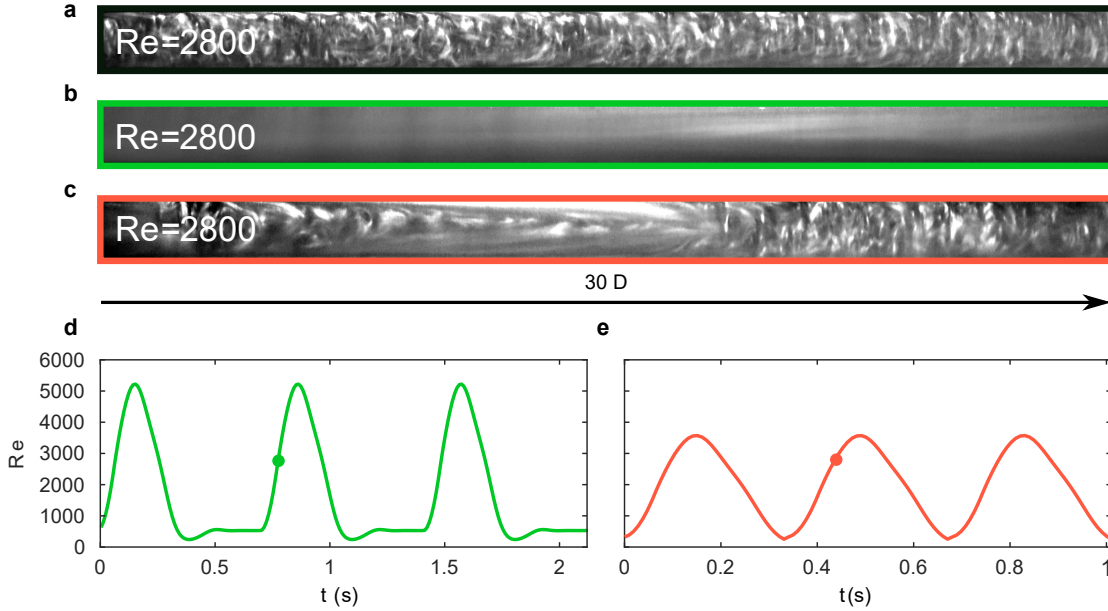
Figure 1: Decay of turbulence in aortic flow. Panel **a** to **c** show three instantaneous snapshots of flows at $Re = 2\,800$. Images capture flow structures in a $30D$ long area located $60D$ downstream of the pipe inlet. In **a** the flow is driven steadily and Re is hence constant. In **b** and **c** flows are driven periodically respectively with (**b, d**) and without (**c, e**) a diastolic rest phase. For the periodic waveforms, the minimum Reynolds number is $Re_{\min} = 270$ in **d** and $Re_{\min} = 180$ in **e**, while the maximum value is $Re_{\max} = 5\,300$ in **d** and $Re_{\max} = 3\,500$ in **e**. The cycle averaged values correspondingly are $\overline{Re} = 1730$ for **d** and $\overline{Re} = 1\,890$ for **e**.
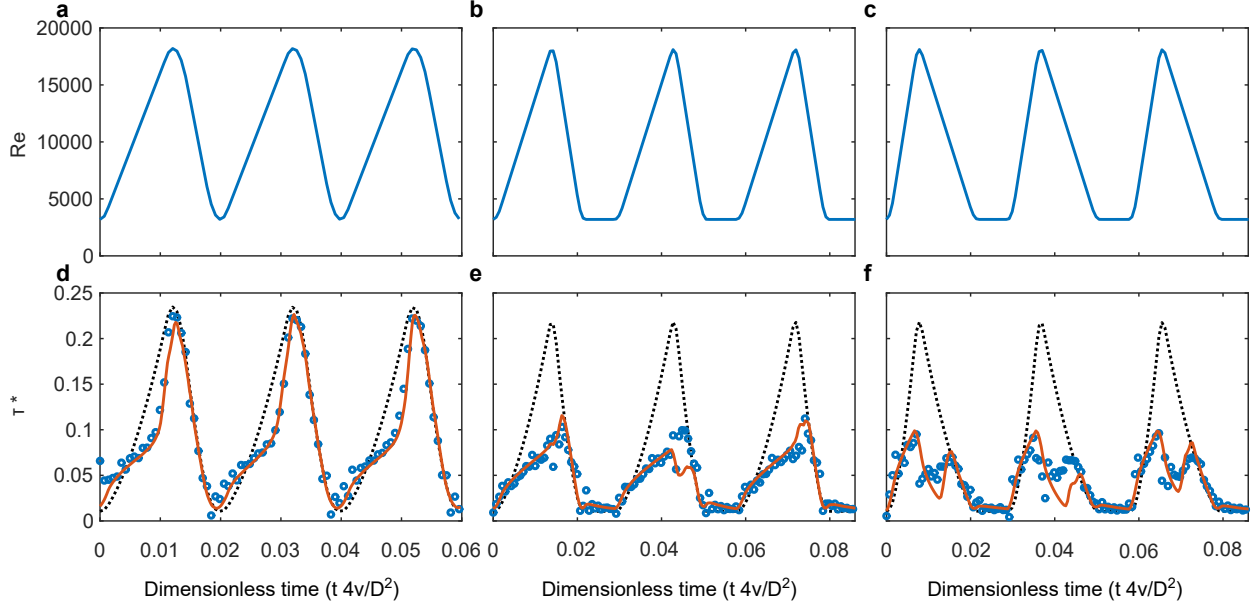
Figure 2: Friction reduction in pulsating flow. Effect of three different cycles on the wall shear stress. In all cases $Re_{\min} = 3\,200$ and $Re_{\max} = 18\,800$. In **a** $\overline{Re} = 11\,000$, in **b** and **c** $\overline{Re} = 8\,600$. The corresponding Reynolds number modulation is imposed in experiments and in direct numerical simulations. Panels **d**, **e** and **f**, display the measured dimensionless wall shear stress τ^* for experiments (blue circles) and DNS (red line). For comparison, the friction associated with the quasi–steady flow is provided by the black dotted line. The quasi–steady values are given by $\tau_{qs}(t) = 0.079 Re(t)^{-0.25} U_m(t)^2 / U_{\min}^2$ (where the Blasius friction scaling is assumed).
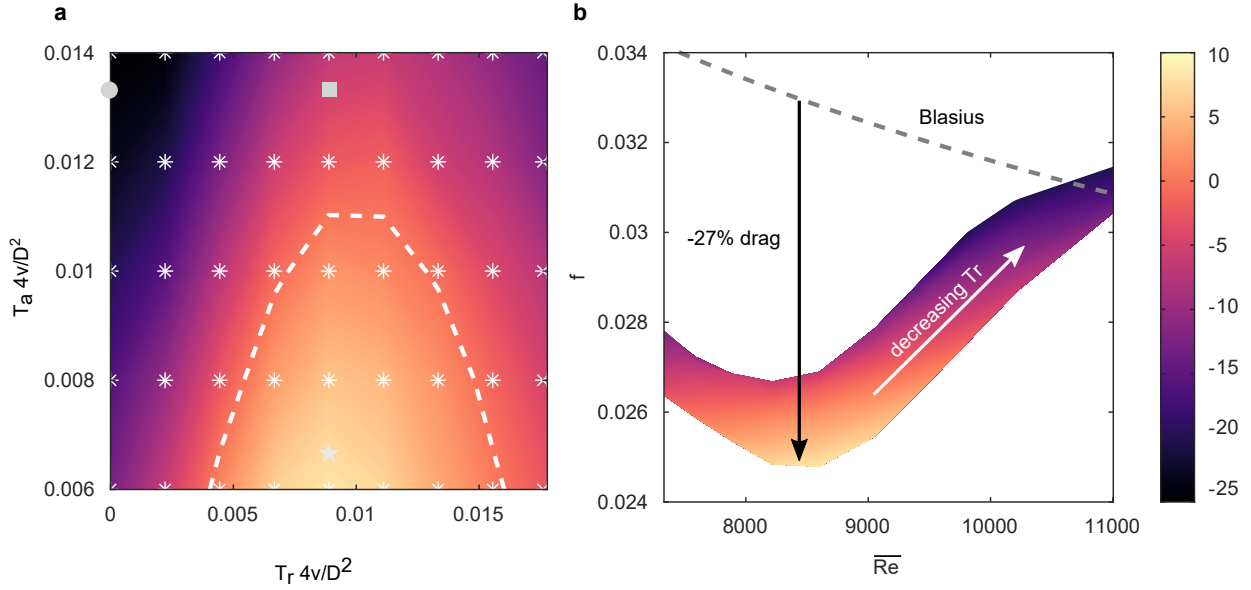
Figure 3: Optimization of power savings. **a** Percentage of the power savings S as a function of the duration of the acceleration T_a and rest phase T_r. The white, dashed line separates the region of positive and negative S. The circle, star and square represent the parameters for the cycles of Fig. 2 **a**, **b** and **c**, respectively. **b** corresponding values of S represented in the traditional f–Re plane, where $f = 2D\Delta p / \left(\rho \bar{U}^2 L \right)$ is the Darcy friction factor. The gray dashed line is the friction level of a steady turbulent flow (Blasius correlation).

Methods

Direct numerical simulations We solve the incompressible Navier–Stokes equations in cylindrical coordinates in a pipe of length $5\,D$ with periodic boundary conditions at the extremities. The equations are written in non–dimensional units by using the pipe radius, $D/2$, as the length scale, the viscous time, $(D)^2/(4\nu)$, as the time scale, and $2\nu/D$ as the velocity scale. They take the following form:

$$\partial_t \boldsymbol{u} + (\boldsymbol{u} \cdot \boldsymbol{\nabla} \boldsymbol{u}) = -\nabla p + \nabla^2 \boldsymbol{u}, \tag{4}$$

$$\boldsymbol{\nabla} \cdot \boldsymbol{u} = \boldsymbol{0}, \tag{5}$$

To impose a time–varying Reynolds number, the mean velocity is updated at every time step, namely

$$U_{m,\text{new}} = U_{m,\text{old}} + \alpha(t)\delta t, \tag{6}$$

where δt is the time step and $\alpha(t)$ is a prescribed acceleration rate. An axial forcing term is then added to the Eq. (4) to enforce that the integral of the instantaneous velocity profile yields the mean flow, *i.e.*

$$U_m = \int_0^1 2u(r)r dr. \tag{7}$$

Simulations were carried out by using the custom, highly–scalable, pseudo–spectral solver *NSPipeFlow*. The codes employs Fourier–Galerkin expansions along the axial and azimuthal directions, and eighth–order, finite central differences for the radial dimension, collocated on a Gauss–Lobatto–Chebyshev grid. The equations evolve in time with a second–order, predictor–

corrector algorithm and a time step dynamically adjusted to satisfy the Courant–Friedrich–Lewy condition. Typical values of the time step size in our simulations range from 10^{-8} to 10^{-10} viscous units. For further details about the code implementation, we refer the reader to Lopez *et al.* [32]. As the Reynolds number changes over time by more than an order of magnitude, the code can adaptively change the grid spacing to match the required spatial resolution needs. More specifically, the adaptive grid method we have implemented ensures that the spatial resolution in the axial and azimuthal directions is consistently below 7.5 wall units, whereas the maximum and minimum spacing in the radial direction is below 3 and 0.1 wall units, respectively. This spatial resolution is more stringent than that customarily used in DNS studies of pipe flow at steady Reynolds numbers. Typical values found at the minimum and maximum Reynolds numbers are given in Table Extended Data 1.

The number of cycles needed to achieve statistical convergence depends on the pulsation waveform. For the case shown in Fig 2d, cycles have little variation, and convergence occurs fast. Statistics were computed in this case using four cycles. For the cases shown in figures 2e y f, there is more variability among cycles, and it is necessary to average over more cycles to obtain converged statistics. For the waveform shown in Fig 2e, statistics were obtained averaging over nine cycles, whereas, for the waveform shown in Fig 2f, 14 cycles were used.

Experimental set–up We employ a large scale, customized syringe pump (sketched in Fig. Extended Data 1) to control precisely the flow rate and hence impose an arbitrary modulation of the Reynolds number. The test section consists of a 7 m long, precision bore glass pipe (Duran,

KPG, internal diameter $D = 30 \pm 0.01$ mm) made by joining 1 m long segments with custom PMMA flanges (in the experiments of Fig. 1 the test section consists of a single pipe segment with $D = 10 \pm 0.01$ mm and length 1.2 m). Water flows through the pipe into a reservoir as the syringe pump is displaced by a linear actuator driven by a servomotor (Festo, ESBF-BS-80-1500-15P and Festo, EMMS-AS-70-M-LS-RS, not shown in Fig. Extended Data 1). A PC is used to control the motor and thus the plunger speed within an accuracy of ± 0.01 mm/s. The syringe has an internal diameter of $D_c = 125 \pm 0.11$ mm and total length $L_c = 1500 \pm 0.1$ mm, corresponding to a maximum run time of ≈ 870 advective time units (D/U) for the chosen pipe diameter. Turbulence development is ensured by perturbing the flow at the pipe inlet with a pin and letting the flow develop for $60\,D$. Differential pressure is measured over the subsequent $120\,D$ with a carefully calibrated pressure transducer, full scale 2.5 kPa. The wall taps (diameter $d = 0.5$ mm) are drilled through the PMMA flanges and have been polished to remove any burr. Water temperature is monitored at the outlet of the pipe with a Pt–100 probe (indicated as T in Fig. Extended Data 1) and typically is held constant within $\pm 0.05\,°$C. In a typical measurement run the desired flow rate wave form is repeated cyclically while traversing the available stroke length. Temperature is measured in real–time in order to compute the correct motor speed and hence imposing the correct Reynolds number. The control and acquisition frequency are set to 50 Hz. Depending on the period duration single runs consists of between 10 and 12 cycles. To ensure a proper statistical representation of the unsteady friction each run is then repeated several times (100 times for the results of Fig.2 and 50 times for the parametric study of Fig.3). The pressure signal has been filtered to attenuate oscillations due to setup vibrations by using a cutoff frequency of 5Hz. The first cycle is found to be

20

systematically different from the others it has been excluded from the averaging process. Overall, the drag reduction R and the power savings S are estimated with a 2–σ accuracy of $\pm 1.8\%$ and $\pm 2.2\%$, respectively.

Calibration In order to ensure repeatable and accurate differential pressure measurements we calibrate the pressure sensor immediately before starting a batch of measurements (a typical batch consists of 10 runs with a minimum of 10 cycles each). For the calibration we measure the pressure drop along the test section Δp for five values of the Reynolds number Re. Each steady measurement is repeated five times and the values of Δp, the piston speed in the cylinder U_c and water temperature T are recorded. The reference value of Δp is computed for each Re by using the Blasius formula,

$$\Delta p = 0.316 Re^{-0.25} \frac{1}{2} \rho U^2 \frac{L}{D}, \tag{8}$$

where $U = U_c D_c^2 / D^2$ is the flow mean velocity in the pipe, D_c is the diameter of the cylinder, L is the length of the test section and ρ is the density of water derived from the temperature T by following the procedure described in [?]. As a result, a calibration curve is obtained to convert the sensor output (in Volts) to a differential pressure in Pascal. To assess the validity of the calibration we compute the residuals of the linear fit and take the maximum value. In the case of the optimal cycle (Fig. 2, **c** and **f**) we find a maximum deviation of ≈ 10 Pa, which is well representative of the values found throughout the experimental campaign.

Standard deviation of mean pressure and flow rate measurements. The mean pressure drop during a cycle is estimated by taking the sample average of the signal $\Delta p(t)$, namely

$$\overline{\Delta p} = \frac{1}{N} \sum_{i=1}^{N} \Delta p_i, \tag{9}$$

where Δp_i is the i-th sample $\Delta p(t_i)$ and N is the number of samples per cycle. The pressure signal recorded for the optimal waveform is reported in Fig.Extended Data 2 **b**. The blue curves correspond to 100 instantaneous cycles and the phase average is shown in red. For comparison we superimpose the computed pressure drop from DNS (dotted line). (Fig.Extended Data 2 **a** shows the corresponding time dependence of the Reynolds number based on the recording of the piston position).

Using Eq.(9) we determined the mean pressure for all 100 cycles and found that the standard deviation between cycles amounts to 2.9% of the mean. This value provides an upper bound on the measurement error involved. Here it has to be taken into account that, due to the unsteady, chaotic nature of the flow consecutive cycles start from different initial conditions, which leads to a natural variation of cycle averaged quantities such as mean pressure. Hence the standard deviation between cycles would be expected to be non-zero even in the absence of measurement error. The error of the mean flow rate $\overline{Q}$ can be estimated from positioning measurements of the piston and the manufacturing accuracy of the piston cylinder, to be 0.6%. For the power input curves, Fig.Extended Data 2 **c**, the standard deviation surmounts to 3.1% .

Computing drag reduction from experimental measurement The drag reduction rate R can be computed by integrating Eq. (1) integer multiples of the period T of the waveform.

$$\int_0^{mT} \rho \frac{dU(t)}{dt} dt = -\int_0^{mT} \left(\frac{\Delta p(t)}{L} + \frac{4\tau_w(t)}{D} \right) dt, \qquad (10)$$

where we assume incompressible flow and make use of the fact that the integral of the bulk flow over a period is zero

$$\int_0^{mT} \frac{\Delta p(t)}{L} dt = -\int_0^{mT} \frac{4\tau_w(t)}{D} dt, \qquad (11)$$

We can therefore rewrite Eq. (2) to express the drag reduction rate R in terms of the time averaged pressure and hence

$$R = \frac{\Delta p_{\text{steady}} - \overline{\Delta p}}{\Delta p_{\text{steady}}}, \qquad (12)$$

where Δp_{steady} is computed for the mean Reynolds number $\overline{Re}$ of the cycle by using the Eq. (8).

As a consequence, the standard deviation in $\overline{\Delta p}$ (2.9% in case of the optimal cycle) provides an upper bound for the uncertainty in R.

Estimation of the power saving Estimating S is also quite straightforward, as it requires taking time averages of the power $P(t) = \Delta p(t)Q(t)$, where $Q(t)$ is the volume flow rate and using Eq.(3, main text), reported here for clarity:

$$S = \frac{P_{\text{steady}} - \overline{P}}{P_{\text{steady}}}. \qquad (13)$$

The accuracy of S can be estimated in the same way we described for R. We compute the mean power $\overline{P}$ for each of the 100 cycles and then estimate the standard deviation between the cycles. We find a value of 3.2%, which also represents of the accuracy of S since in Eq.(13) $\overline{P}$ is the only uncertain quantity.

Comparison with DNS Selecting the optimal waveform (Fig. 2c) we compare the values of R and S obtained from experiment to those observed in direct numerical simulations. The histograms of the 100 cycles measured experimentally are shown in Fig. Extended Data 3 (a) and (b). Since (due to computational costs) a much smaller number of cycles have been simulated, instead of histograms, we computed the mean values for the DNS for R and S (orange dashed lines).

Finally, we report in table Extended Data 2 the average values for R and S for all three waveforms of Fig. 2 for experiments and DNS and they turn out to be in close agreement.

Waveforms The waveforms considered are composed of linear ramps in Re and periods of constant flow rate. Throughout the experiments the minimum and maximum Re are held constant and equal to $Re_{\min} = 3\,200$ and $Re_{\max} = 18\,800$, respectively. The combined duration of acceleration and deceleration T is always fixed to 4.5 s, while the duration of the acceleration and rest phase are respectively varied in the intervals $T_a \in [1.35, 3.15]$ s and $T_r \in [0, 4]$ s. To avoid abrupt changes in the piston acceleration, the sudden slope changes, that occur at the transition points from acceleration to deceleration to rest phase, have been locally smoothed with a moving average filter of width 0.8 s (cf. Fig. 2 (a), (b) and (c)).

Data availability

The datasets generated and analyzed during the current study are freely available in the Zenodo repository, https://doi.org/10.5281/zenodo.7828996.

Code availability

The numerical simulations were conducted with the open source code nsPipeFlow, distributed under the terms of the GNU General Public License version 3. A detailed description of the code and user guide is provided in reference 30. The code version used in this study and an initial condition to start the simulations are openly available in the Zenodo repository, https://doi.org/10.5281/zenodo.7828996.
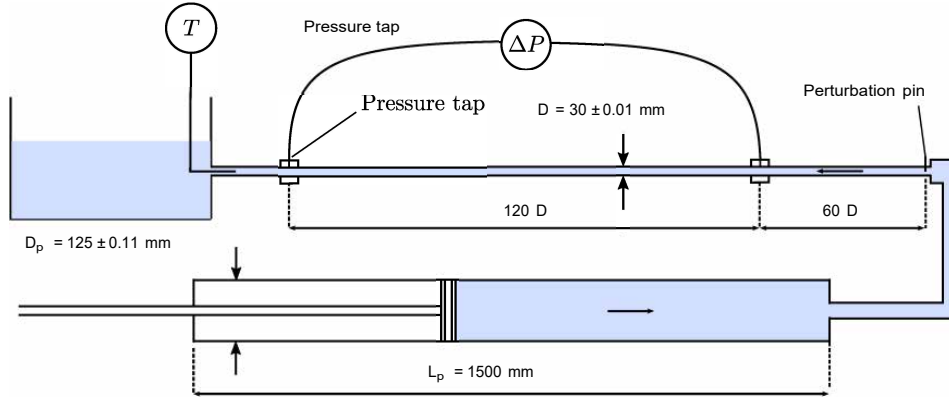
Figure Extended Data 1: Sketch of the experimental setup. Drawing not to scale.

Re	$\min \Delta_r^+$	$\max \Delta_r^+$	$\Delta_{(R\theta)}^+$	Δ_z^+	δ_t
3 200	0.053	2.44	7.06	5.62	$4.80 \cdot 10^{-8}$
18 800	0.016	2.70	7.23	7.20	$1.91 \cdot 10^{-8}$

Table Extended Data 1: Parameters used in the direct numerical simulations. From left to right: Reynolds number Re based on the mean velocity, minimum and maximum radial resolution (in inner units), azimuthal resolution (in inner units), axial resolution (in inner units) and average time step size δ_t.

Cycle	R_{exp}	R_{dns}	S_{exp}	S_{dns}
(a)	-4.4	0.6	-30.4	-29.0
(b)	22.5	22.4	-3.0	-3.1
(c)	27.4	27.9	9.0	6.9

Table Extended Data 2: Comparison between the values of R and S in percentage for the waveforms of Fig.2 obtained from experiments and DNS.
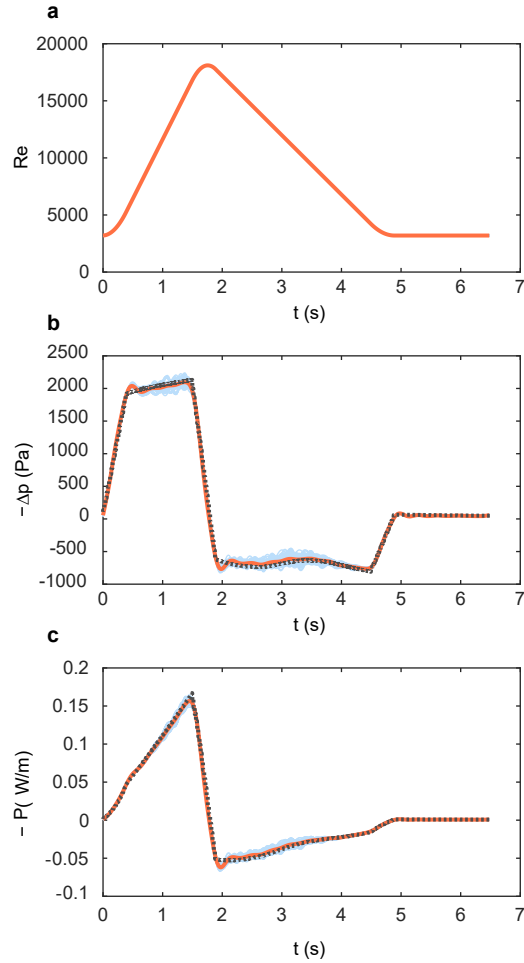
Figure Extended Data 2: Waveform, pressure and power signal. Signals from the optimal cycle (Fig. 2c) measured in experiments. (a) Waveform based on the linear piston speed and (b) pressure drop Δp measured over the test section. The signal from all the 100 cycles measured is shown in blue, while the phase average is represented in orange. The number of samples per cycles is $N = 325$. For comparison, we report also the pressure drop computed with the DNS for the same cycle (gray dotted line). In this case the signal is obtained by phase-averaging the available 8 cycles. (c) The power input for the same waveform. The values for the 100 cycles in experiments are shown in blue, the ensemble average in red and the power input in DNS is given by the grey doted line.
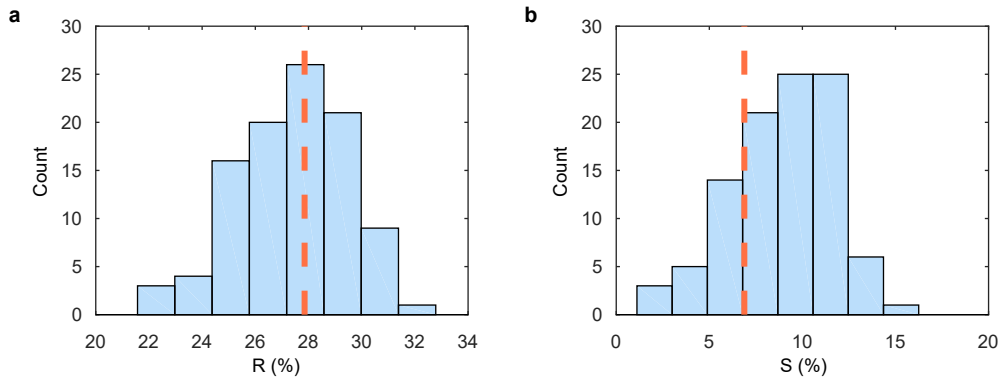
27

Figure Extended Data 3: Comparison of the values of (a) R and (b) S between experiments (blue histogram) and DNS. For the optimal cycle (Fig. 2c, main text) the histogram shows the distribution of the values obtained from 100 runs. The orange, dashed line shows the mean of the available corresponding DNS cycles.
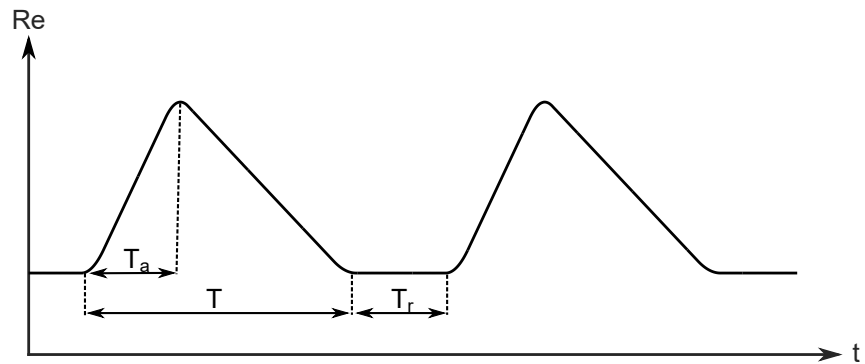

Figure Extended Data 4: Definition of the flow cycle used in the experiments of Fig.2 and Fig.3.